

X-ray2CTPA: Generating 3D CTPA scans from 2D X-ray conditioning

Noa Cahan^{1,*}, Eyal Klang², Galit Aviram³, Yiftach Barash⁴, Eli Konen⁴, Raja Giryes¹, and Hayit Greenspan^{1,5}

¹Faculty of Engineering, Tel Aviv University, Tel-Aviv, Israel

²Division of Data-Driven and Digital Medicine, Department of Medicine, Icahn School of Medicine at Mount Sinai, New York, NY 10029, United States.

³Department of Radiology, Tel-Aviv Sourasky Medical Center and Tel Aviv University School of Medicine, Israel.

⁴Department of Diagnostic Imaging, Sheba Medical Center, Ramat Gan, Israel affiliated with the Tel Aviv University, Tel Aviv, Israel

⁵Department of Radiology, Icahn School of Medicine, Mount Sinai, NY

*Corresponding author. E-mail: noa.cahan@gmail.com

ABSTRACT

Chest X-rays or chest radiography (CXR), commonly used for medical diagnostics, typically enables limited imaging compared to computed tomography (CT) scans, which offer more detailed and accurate three-dimensional data, particularly contrast-enhanced scans like CT Pulmonary Angiography (CTPA). However, CT scans entail higher costs, greater radiation exposure, and are less accessible than CXRs. In this work we explore cross-modal translation from a 2D low contrast-resolution X-ray input to a 3D high contrast and spatial-resolution CTPA scan. Driven by recent advances in generative AI, we introduce a novel diffusion-based approach to this task. We evaluate the model's performance using both quantitative metrics and qualitative feedback from radiologists, ensuring diagnostic relevance of the generated images. Furthermore, we employ the synthesized 3D images in a classification framework and show improved AUC in a PE categorization task, using the initial CXR input. The proposed method is generalizable and capable of performing additional cross-modality translations in medical imaging. It may pave the way for more accessible and cost-effective advanced diagnostic tools. The code for this project is available: <https://github.com/NoaCahan/X-ray2CTPA>.

Introduction

Chest X-rays or chest radiography (CXR) are pivotal in emergency diagnostics due to their speed and accessibility, offering a cost-effective, non-invasive solution¹. However, their 2D nature and lower soft tissue contrast limit their diagnostic ability compared to CT scans, which provide comprehensive 3D views of the various tissues including the lungs, bone and soft tissue, albeit at higher costs and radiation exposure^{2,3}. CTPA scans, a specialized form of CT with fast contrast material injection, further enhance blood vessels but may be less suitable for certain groups, including those with severe contrast allergies, or renal failure. In this work, we wish to demonstrate the use of advanced generative AI schemes for cross-model translation. In our main focus scenario, we build a system to translate 2D X-ray images into 3D CTPA scans. We explore the quality of the generated scans and their promise for earlier detection of findings in the initial CXR data, specifically focusing on Pulmonary Embolism (PE) classification. Finally, We show the generalization of the developed cross-model translation scheme using the LIDC dataset, demonstrating possible transition from CXR to synthetic thoracic CT images.

We address the classification of pulmonary embolism (PE) as present or absent, from CXR imaging as a case study in order to demonstrate the potential of transferring CXR to CT. PE is a life-threatening condition where a blood clot that develops in a limb vein travels to the pulmonary arteries where it suddenly blocks the blood flow. The gold standard for PE diagnosis is CTPA – a 3D lung CT with contrast injection. However, the use of CT is associated with exposure to ionizing radiation, and iodinated contrast, requires expensive scanners and qualified staff to operate them, and radiologists to interpret. The number of CTPAs performed continues to rise, with only 5-15% of them being positive for PE diagnosis⁴. Therefore, there is a need in the modern health care system to develop a simple, easy, fast and objective tool for diagnosing this common but life-threatening disease of PE, based on low-radiation-low-cost data, which is routinely collected for the investigation of patients with cardio-respiratory complaints utilizing advanced AI-based tools. In the emergency department, almost every patient with cardiac or respiratory issues undergoes a CXR, despite its lower tissue resolution and limited information for PE diagnosis. This underscores the opportunity to enhance the utility of CXR imaging in PE detection through innovative approaches.

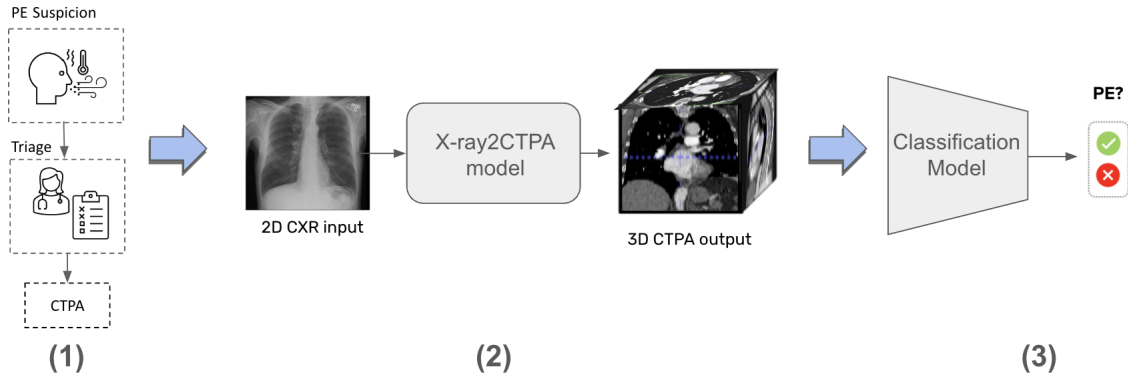


Figure 1. The outline of our study. The first stage was to establish the cohort and collect the dataset. Our pipeline for PE classification from CXRs consisted of collecting patients who underwent both chest X-rays and CTPA scans. The PE diagnosis label was collected from the CTPA scan’s radiologist report. At a second stage, once the X-ray2CTPA diffusion model is trained, the corresponding CTPA scans are generated from their matching CXRs. Finally, the generated data is used for training and testing a PE classifier for PE diagnosis. (Icon images from Microsoft PowerPoint 2023.)

Recent years have witnessed remarkable advancements in Generative AI, a field dedicated to empowering machines with the ability to create novel, realistic data using frameworks such as Generative Adversarial Networks (GANs) and diffusion models. From crafting stunning photorealistic images to composing original music and even translating languages fluently^{5,6}, generative models have demonstrated their versatility and potential across diverse domains. However, in the field of healthcare and medical imaging, the integration of cross-modal generative AI, especially in 3D imaging, is still in an early stage and confronts significant challenges⁷. Specifically, the synthesis of high-resolution CTPA scans from an extremely limited number of 2D scan slices and furthermore from a single 2D image is a yet unaddressed challenge.

A limited number of recent works have shown possible transition from digitally reconstructed Radiographs (DRRs) to CT volumes^{8,9}. Here, the input is synthetic CXR data that is generated from a CT’s 2D projection. The use of this synthetic approach simplifies the problem and makes these works somewhat remote from the true clinical setting. The reason is that DRRs inherently contain more information compared to actual CXR scans, and they are inherently aligned with the CT data from which they are extracted. This intrinsic registration and enhanced information content potentially ease the conversion task from DRRs to CT, when contrasted with using real CXRs. Furthermore, we are not aware of any existing work that has demonstrated the potential of using the generated synthesized scans for a specific diagnostic application.

Bridging this gap, our study collects a unique dataset of 900 patients who underwent both a 3D CTPA and a 2D CXR within 24 hours, and were suspected to have PE. The CTPAs and the CXRs are paired so that each pair belongs to the same patient. The PE diagnosis label (positive or negative), was collected from the CTPA scan’s radiologist report of the CTPA. We use the cross-modality paired scans to train the X-ray2CTPA diffusion model (details in the Methods Section). In a following stage, once the X-ray2CTPA diffusion model is trained, synthesized "matching" CTPA scans (with or without PE) are generated from an input CXR image and used for training and testing a PE classifier for PE diagnosis. **Fig. 1** presents the study design used for this research.

It is our hypothesis, that the synthesized data can support PE categorization from the initial CXR imaging phase. The generation of CTPAs from CXR images may enhance the specificity of diagnosing PE by CXRs, potentially decreasing the number of patients who require actual CTPA scans, with higher yield (positive PE scans-in higher percentage). Our model can predict the presence of PE on CTPA, leading to a reduction of negative CTPA scans, thus saving the radiation-related health burden and financial health resources currently spent on the performance of redundant negative CTPAs, while ensuring a safe exclusion of PE without the need of CTPA. Note that the generated CTPAs are not clinical substitutes for actual CTPA scans. They can be viewed as "pseudo-CTPA" information that can provide valuable preliminary data prior to deciding on conducting a comprehensive real CTPA examination.

Our contributions through this work are as follows:

1. **Innovative Cross-Modal Translation.** We introduce a novel method, leveraging the power of diffusion models, CLIP Vision encoder and adversarial guidance to translate 2D CXR images into 3D CTPA scans. This method maintains high fidelity and diagnostic relevance, as confirmed by both quantitative metrics and qualitative feedback from radiologists.

To the best of our knowledge, this is the first research that uses real CXR and CTPA paired data for the application of CXR to CTPA translation.

2. **Potential earlier identification of PE in CXR.** We demonstrate the use of cross-modality synthetic data generation to increase the performance of PE identification in CXR images. By generating high-quality synthetic 3D images, we show results for improved classification accuracy for PE, increasing the specificity of diagnosing PE.
3. **Generalizability.** The proposed method demonstrates potential for broader applications in medical imaging, paving the way for more accessible advanced diagnostic tools.

Related work

3D Image generation diffusion models in medical imaging. Image generation is one of the primary objectives of diffusion models, which has been widely applied in a variety of styles, including generating synthetic 3D medical images¹⁰. Medical Diffusion¹¹ excelled in creating high-quality medical 3D data in an unconditional setting. There are also many 3D conditional models. We list here a few but there are many more: DISPR¹² involves reconstructing 3D cells from 2D cell images and their corresponding segmentation mask, Med-DDPM model¹³ is a conditional diffusion model for semantic 3D medical image synthesis. Make-A-Volume¹⁴ leverages latent diffusion models for cross-modality 3D brain MRI synthesis and GenerateCT¹⁵ introduced a novel approach that combines transformers and diffusion models for generating CT volumes conditioned on free-form medical text prompts. Our work represents a departure from existing works, where conditioning often relies on text prompts trained on extensive datasets or involves adding directly correlated information, such as segmentation masks or structural guides, to the generated image. In contrast, in our research the conditioning is on a different modality altogether.

CXR to CT generation. CXR to CT conversion is an under-explored area of research and there are not many works that attempt to solve this problem. X2CT-GAN⁸ and its extension - XprospeCT¹⁶, explores the use of Generative Adversarial Networks (GANs) for reconstructing 3D CT volumes from biplanar 2D CXRs. MedNeRF⁹ introduces a deep learning model for reconstructing CT projections from as few as a single-view CXR. This approach utilizes a neural radiance field (NeRF) architecture to learn a continuous representation of CT scans. The model effectively disentangles the shape and volumetric depth of surface and internal anatomical structures from 2D images. For both papers, the CXRs used are synthetic constructions from CTs called DRR, which are similar but not identical to real CXRs. This is due to the lack of a publicly available dataset of paired CXR and CT. We argue that the task of converting DRRs to CT scans is less complex than our task because DRRs inherently possess more information than CXRs. Also, DRRs are naturally aligned and registered with CTPAs due to the way they are constructed.

A concurrent work, X-Diffusion¹⁷ is perhaps the most related to our approach. It generates 3D MRI volumes from either a single slice of the MRI or from a registered Dual-energy X-ray Absorptiometry (DXA) which is a single image data modality that is similar to X-ray but includes other non-bony information such as tissue mass. Unlike their framework, the challenges in our problem setting are heightened by the limited size of our dataset, the extremely low resolution in the CXR scans, and the fact that, in our case, the two data modalities are completely distinct and unaligned or unregistered. To the best of our knowledge, our model is the first one to convert matching 2D X-rays to 3D CT.

Results

The diffusion models were pretrained on the RSPECT dataset¹⁸. Then, the diffusion model was fine-tuned on our dataset in a two-stage setting. First, the model was fine-tuned in an unconditional manner, without any CXR conditioning. In the second stage, the CXR conditioning was added, and the model was further trained. Even though the datasets were relatively small, we found that each model converged and generated realistic synthetic images without a lot of hyperparameter finetuning. We present below various quantitative and qualitative evaluations of our proposed approach.

Quantitative Results

To assess sample quality, we conduct quantitative evaluations utilizing various metrics. While these metrics are commonly employed and generally align with human judgment, they are not flawless indicators. There is ongoing exploration of improved metrics in evaluating sample quality, which remains an open challenge. In essence, appraising the visual accuracy of synthetic images, particularly within medical imaging, continues to be a complex task where small details may hold significant importance¹⁹. Keeping in mind these limitations, we evaluated the quality of the generated CTPA volumes using four metrics:

1. Fréchet Video Distance (FVD): FVD was proposed by Salimans et al.²⁰. It quantifies the dissimilarity between generated and real CTPA volumes by extracting image features using the I3D model²¹, which is well suited to video datasets. This metric is only partially suited and holds inherent limitations as it is not fully suited to medical datasets.

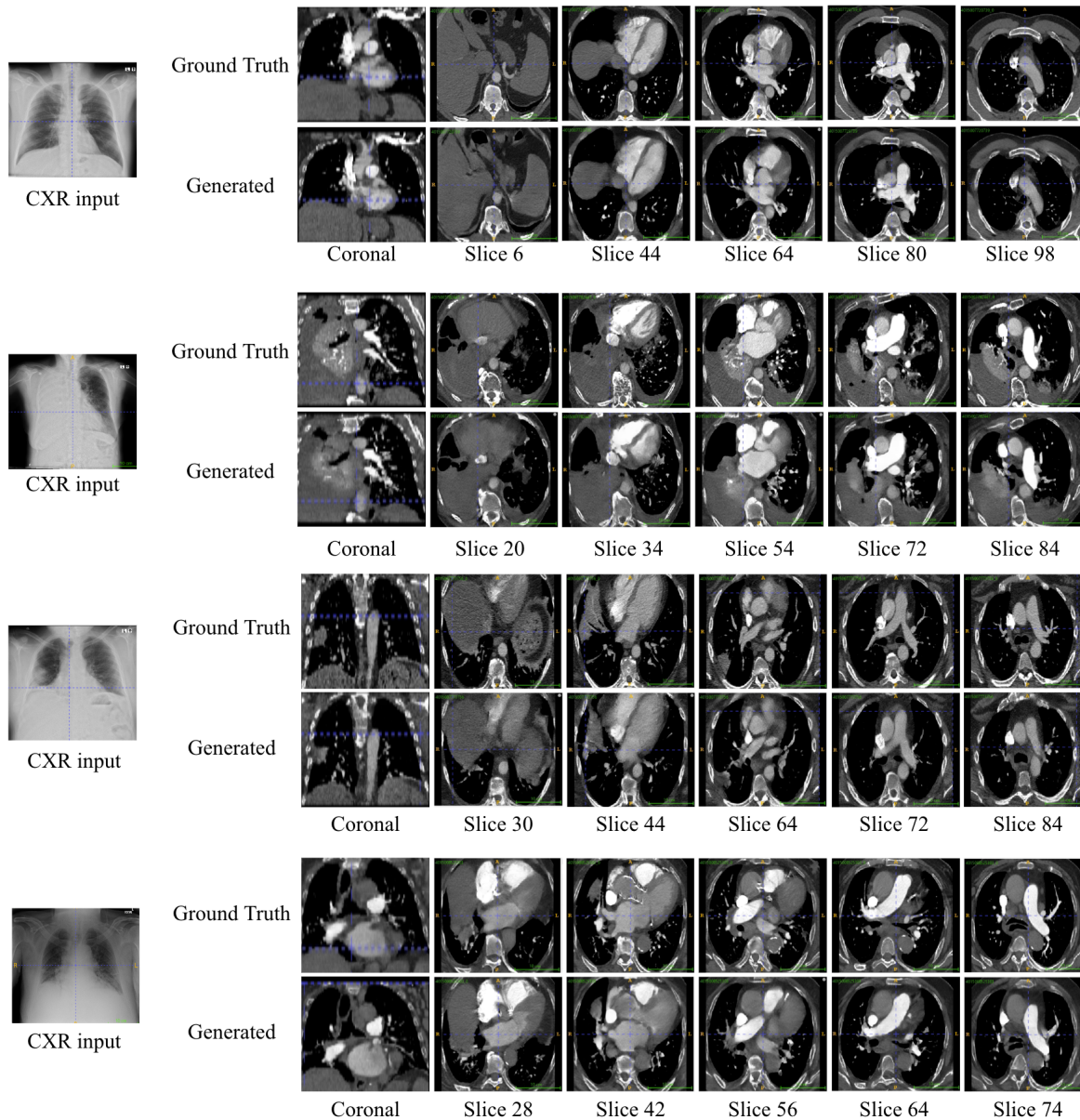


Figure 2. Qualitative results. We show examples of CXR to 3D CTPA Generation with an X-ray2CTPA model. Shown are four randomly selected generated 3D-CTPA samples from the test set, synthesized from a 2D CXR input. We compare slices from the generated 3D-CTPA scan to the ground truth samples. For simplicity, we present five key slices from the whole 3D-scan. The input CXR is presented as well, along with its matching coronal slice from the matching CTPA and generated 3D-CTPA. Note: throughout the paper the axial CT images appear slightly deformed. This is due to the preprocessing of the data and region of interest selection. (We elaborate on this in the Dataset Section.)

2. PSNR: PSNR is often used to measure the quality of reconstructed digital signals²². The high dynamic range of the CTPA scan makes PSNR a good criterion for image quality evaluation.
3. SSIM: SSIM is a metric to measure the similarity of two images, including brightness, contrast and structure²³. Compared to PSNR, SSIM better matches human’s subjective evaluation.
4. LPIPS²⁴: LPIPS essentially computes the similarity between the activations of two image patches for some pre-defined neural network. This measure has been shown to match human perception well. A low LPIPS score indicates that image patches are perceptually similar.

We computed these metrics by evaluating the generated samples against their corresponding ground truth samples in our test set. **Table 1** presents the quantitative generation results for the CTPA dataset.

Table 1. Quantitative evaluation of the synthesized test set samples using different metrics. FVD scores are multiplied by 10^3 .

Dataset	Metric			
	FVD ↓	PSNR ↑	SSIM ↑	LPIPS ↓
CTPA	0.29 ± 0.22	19.41 ± 0.96	0.58 ± 0.08	0.14 ± 0.04

Qualitative Results

In **Fig. 2** we show visual examples of generated scans. The results demonstrate that the generated scans seem anatomically correct, realistic and consistent between sequential slices. **Fig. 2.** visualizes key slices from four randomly selected generated samples from our held-out test set and the corresponding slices compared with the ground truth scan. As can be seen, the slices are similar but small variations exist compared to the ground truth samples. These differences will be further discussed in the following sections. In addition, the input CXRs for the generated samples are depicted, along with the corresponding coronal example slice from the ground truth and the matching slice from the generated sample. It is evident that general anatomical structure is preserved between the generated sample and ground truth and matches the CXR input.

We next compare generated PE examples from the synthesized data with their corresponding ground truth. **Fig. 3** presents the results. As observed, the X-ray2CTPA model successfully generates findings consistent with PE diagnosis. Although some variations in manifestation and location may occur in the generated PE findings compared to the ground truth samples, the overall results are similar. We hypothesize that our model captures the statistical essence of the ground truth, even if the resulting scans are not identical. This hypothesis is supported by the results presented in the following sections.

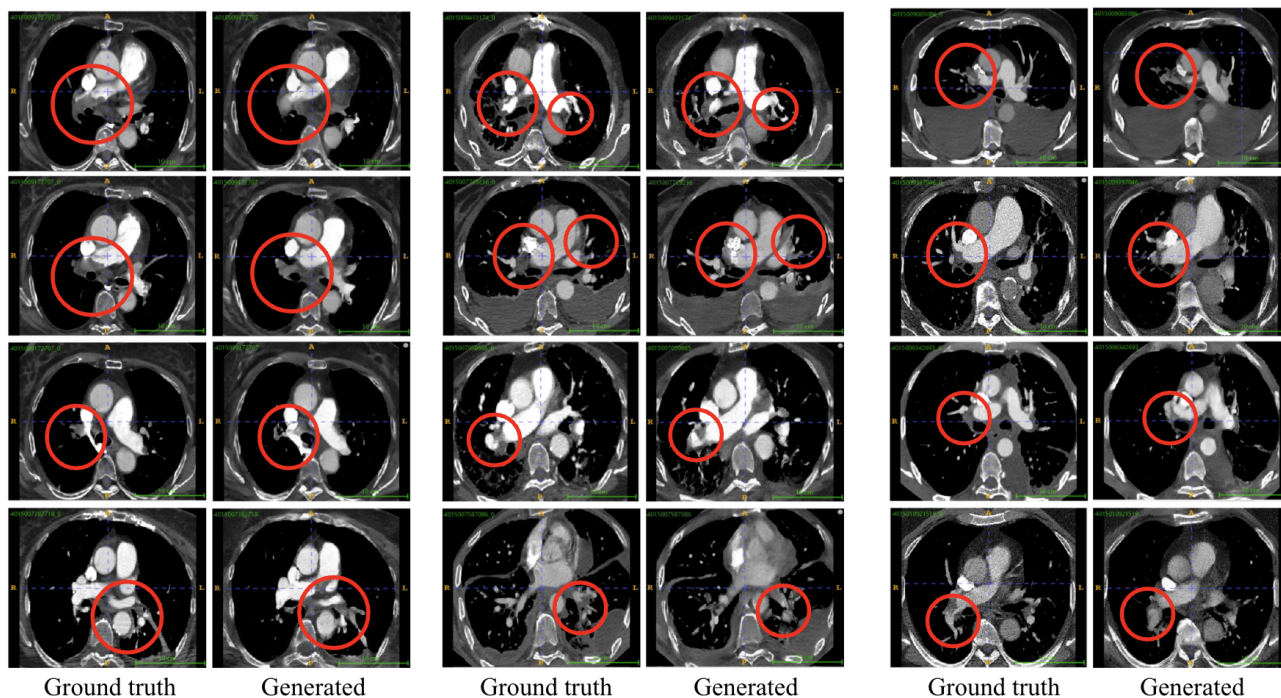


Figure 3. Visual results of generated PE clots examples. Presented are different 2D slices from generated 3D CTPA samples from our test set, which contain PE clots, compared to their ground truth 2D slices. The PEs are marked with a red circle.

We conducted a short expert evaluation study, with the generated scans evaluated by two expert Radiologists. First, experts were presented with 20 CTPA volumes, comprising an equal mix of 10 real and 10 synthetic ones. Readers were tasked with assessing the visual quality of these volumes and determining whether each volume was real or synthetic. Both readers accurately distinguished between most synthetic and real volumes, citing the inferior image quality of the synthetic scans

compared to the real scans as the primary reason. As a followup, we asked the experts to rate the synthetic images in terms of anatomic correctness and slice consistency. The readers were asked to rate 10 generated images from the test set. All readers rated the scans as mostly realistic with only minor unrealistic areas. In addition, the images were considered consistent across slices with most images assessed as exhibiting only minor or no anatomic inconsistencies. We conclude from this initial study that our architecture can generate synthetic images that appear somewhat realistic to radiologists but further work needs to be done if we wish to achieve realistic-looking images. We hypothesize that better-quality output images can be generated once more data is used in the training phase. The small inconsistencies may be mitigated by adding a super-resolution stage, increasing the sample size, or using a pre-trained diffusion model and adapting it to our problem using tools such as ControlNet²⁵.

Ablation study on model architecture choices

Table 2 evaluates several design choices and the contribution of different network components. We examined different loss functions as alternatives for the model training. In addition to L_1 loss which minimizes the pixel distance between the generated sample and the ground truth, we compared the use of adding perceptual loss²⁴, adding adversarial loss using a discriminator and classification loss. As can be seen from the results, adding the perceptual loss improved the results compared to using only L_1 loss. However, while the addition of adversarial and classification loss did not enhance the quantitative metrics, they both played important roles for our model. Adding the adversarial loss resulted in more visually realistic samples. The classification loss improved the classification results. This is presented in Fig. 4. Additionally, we modified the pretraining process to include the RSPECT dataset not only in as an unconditional dataset for CTPA scans but also in a conditional setting by incorporating synthetic CXR images or digitally reconstructed Radiographs (DRRs) created from the CTPA scans. Adding this pretraining step highly boosted our performance by all metrics.

We also present the results of experiments that failed to achieve optimal outcomes. We attempted to use classifier-free guidance (CFG) for both CXR conditioning and class label conditioning, but neither approach improved the results. Additionally, we experimented with variations in sample size. The spatial resolution of 512 likely yielded sub-optimal results due to our small sample size, and the resolution of 128 failed due to the limitations of the pre-trained VAE we used, which was not trained on smaller image sizes. Lastly, we also attempted to use the pre-trained 3D-VQGAN from medical diffusion¹¹, which was pre-trained on the LIDC dataset, but it failed to improve results on the CTPA dataset.

Table 2. Quantitative evaluation of the synthesized test set samples using different metrics for different model variants. FVD scores are multiplied by 10^3 .

Model Variant	FVD ↓	PSNR ↑	SSIM ↑	LPIPS ↓
Loss				
L1	2.14 ± 0.8	11.61 ± 0.91	0.2 ± 0.06	0.48 ± 0.07
L1 + LPIPS	1.89 ± 0.64	14.78 ± 0.60	0.22 ± 0.07	0.34 ± 0.06
L1 + ADV	2.06 ± 0.63	11.53 ± 0.78	0.2 ± 0.058	0.45 ± 0.052
L1 + LPIPS + ADV	1.94 ± 0.63	14.38 ± 0.77	0.21 ± 0.06	0.36 ± 0.048
L1 + Classifier	2.64 ± 1.75	12.03 ± 0.82	0.2 ± 0.05	0.50 ± 0.06
Classifier Free Guidance				
CFG	2.16 ± 1.78	11.57 ± 0.68	0.19 ± 0.04	0.48 ± 0.03
label CFG	2.05 ± 0.78	11.48 ± 0.81	0.19 ± 0.06	0.48 ± 0.06
Sample size				
128 x 128 x 64	2.88 ± 1.2	11.68 ± 0.65	0.22 ± 0.09	0.55 ± 0.05
512 x 512 x 32	2.65 ± 0.8	11.88 ± 0.77	0.21 ± 0.08	0.55 ± 0.05
Architecture components				
3D-VQGAN	4.01 ± 1.4	10.89 ± 0.9	0.12 ± 0.07	0.88 ± 0.06
CLIP	3.74 ± 1.2	11.39 ± 0.79	0.14 ± 0.08	0.76 ± 0.05
Full				
X-ray2CTPA	0.29 ± 0.22	19.41 ± 0.96	0.58 ± 0.08	0.14 ± 0.04

In addition to the quantitative results, we also compare the visual differences of using different loss functions (Fig. 4). All

loss functions were trained as a weighted combination with the $l1$ loss. In general, it is evident that the generated samples are like the ground truth, although not identical. Supporting the quantitative results, the LPIPS loss improves both the visual appearances of the generated samples and seem to guide the scans to be closer in structure and color contrast to the ground truth. The pretraining step using the DRRs as conditioning further enhances the LPIPS loss improvements and provides the most realistic images which are also the most close to the ground truth. The classification loss adds distortion to the samples, which is expected as its purpose is only to aid the classification task. The adversarial loss provides very realistic images but, in some cases, the generated sample is derived further away from the ground truth. The weighted combination of all losses (Fig. 4 - "Full") provides the best tradeoff between all losses.

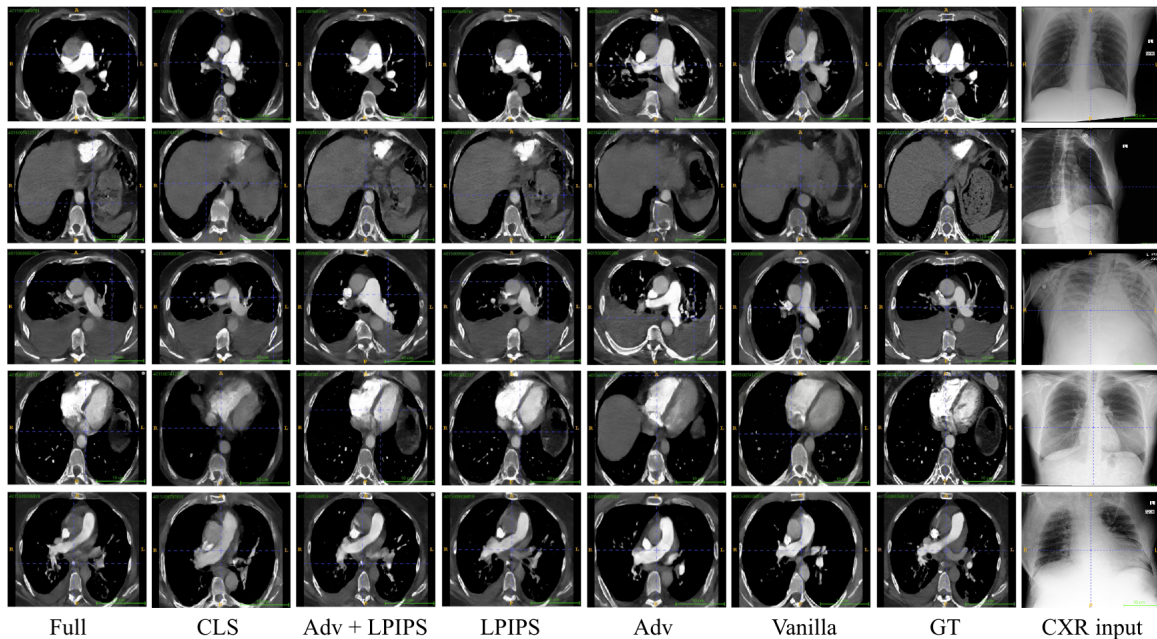


Figure 4. Visual ablation of loss functions used for this study. Presented are different slices from generated 3D CTPA samples from our test set, which were trained using various loss functions and combinations. "Vanilla" = $l1$ loss, "Adv" = adversarial loss, "CLS" = classification loss and "Full" = weighted combination of all losses.

Synthetic 3D CTPAs can be used to enhance PE classification

As part of our evaluation, we aimed to assess the generated CTPA's suitability to be used for a classification task. Specifically, we applied the generated data to the task of PE classification. As mentioned in the Introductory section, CTPA is the gold standard for PE diagnosis, and PE is usually not noticeable on CXRs due to their non-contrast enhanced and 2D nature. We hypothesize that by training the diffusion model with matching CXR and CTPA pairs, an alignment is constructed between the two modalities that can stir the generated 3D-image so that it can improve the classification results compared to a classification using CXRs. **Table 3** presents the results for this classification task.

The classification of PE using unimodal data: CTPA only and CXR only data, are used as our baselines. The results present our sixfold cross-validation analysis, by presenting the average AUC, with a 95% confidence interval, calculated across all folds using the Delong method²⁶. We set our operating point based on the Youden's J-Score statistic that maximizes the sum of sensitivity and specificity on the validation set. For the numerical threshold that separates the predicted classes, we utilized the standard definition of the operating point.

As expected, the real CTPA classification results outperform the CXR results achieving an AUC of 0.827 [95% CI: 0.75-0.92] compared to 0.691 [95% CI: 0.54-0.77]. The classification using the generated CTPAs significantly outperformed the CXR classification results with an AUC of 0.803 [95% CI: 0.72-0.9]. In addition, the specificity and NPV of the model improve as well compared to the CXR classifier. In a clinical context, this outcome suggests a higher number of true negative results, leading to a reduction in unnecessary CTPA scans performed. It is evident that using the synthetic CTPAs enhance performance compared to using solely CXRs. For the CTPAs classification, we used the latent output representation from the 2D-VAE used in our diffusion model. The CXRs were classified using RadImageNet²⁷, a ResNet-50 based model pretrained on millions of radiologic images.

Table 3. Comparing the average AUC scores (with a 95% confidence interval) of the PE classification from CXR, CTPA and Generated CTPAs on our test set.

Model	AUC	Accuracy	Specificity	Sensitivity	PPV	NPV
Baselines						
CTPA only classifier	0.827 [0.75-0.92] \pm 0.05	76.92	78.18	73.91	58.62	87.76
CXR only classifier	0.691 [0.54-0.77] \pm 0.06	71.79	70.91	73.91	51.52	86.67
Generated Data						
Generated CTPA only classifier	0.80 [0.72-0.9] \pm 0.07	74.0	74.1	73.91	54.8	87.0

All results are statistically significant with Kolmogorov–Smirnov test, with $p \leq 0.05$

Generalizability

We wanted to evaluate the ability of our model to generate other modalities in a similar setting. To do so, we fine-tuned our model on an additional dataset. We used chest CT studies from the publicly available Lung Image Database Consortium (LIDC) dataset²⁸. This dataset contains 1010 (thoracic CT) individual studies. We noticed that in addition to the available CT scans, around 290 scans also included matching CXRs. We fine-tuned the model using low rank adaptation (LoRA)²⁹.

The quantitative generation results for the LIDC dataset are presented in **Table 4**. As can be seen, although trained on an extremely low number of samples - the evaluation results are high.

Table 4. Quantitative evaluation of the synthesized test set samples from LIDC dataset. FVD scores are multiplied by 10^3 .

Dataset	Metric			
	FVD \downarrow	PSNR \uparrow	SSIM \uparrow	LPIPS \downarrow
LIDC	0.97 ± 0.71	18.02 ± 2.12	0.53 ± 0.06	0.31 ± 0.07

In addition to the quantitative results we also provide a generation example of one scan compared to its corresponding ground truth. The results are presented in **Fig. 5**.

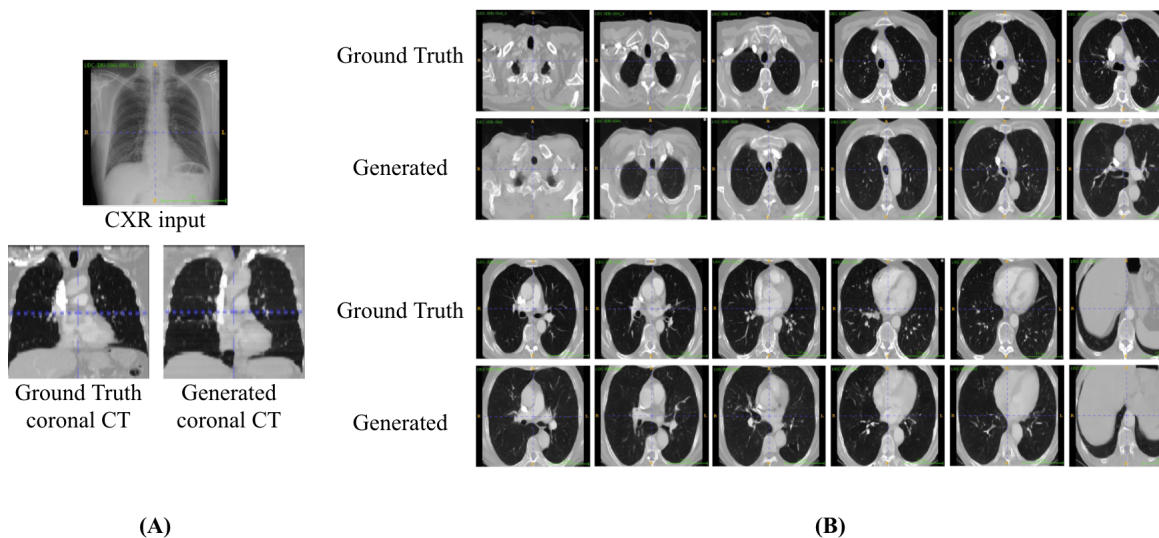


Figure 5. Qualitative Results of CXR to 3D CT Generation with X-ray2CTPA model from LIDC dataset. (A) We present a generated 3D-CTPA sample from the test set, generated from a 2D CXR input. We compare slices from the generated 3D-CT scan to the ground truth sample. (B) The input CXR is presented along with the matching coronal slices from the matching CT and generated 3D-CT. This is the same sample as in the previous figure.

Failed examples

While X-ray2CTPA model can generate high-quality 3D CTPA samples that closely resemble the ground truth in structure and appearance, there are instances where it slightly diverges or fails to accurately replicate the ground truth. Some examples from our test set as presented in **Fig. 6**. The main areas where the model fails are around small veins or when rare abnormalities or additional pathologies (other than PE) are presented. In some of these cases the model generates the pathology in some variant but may replicate it in a wrong location or fail to generate the pathology whatsoever. We hypothesize that this issue may be caused by the high variability nature of the CTPA samples and due to the fact, that in many cases PE is secondary to other patient co-morbidities. We believe that training the model with a larger dataset may solve this issue in future work.

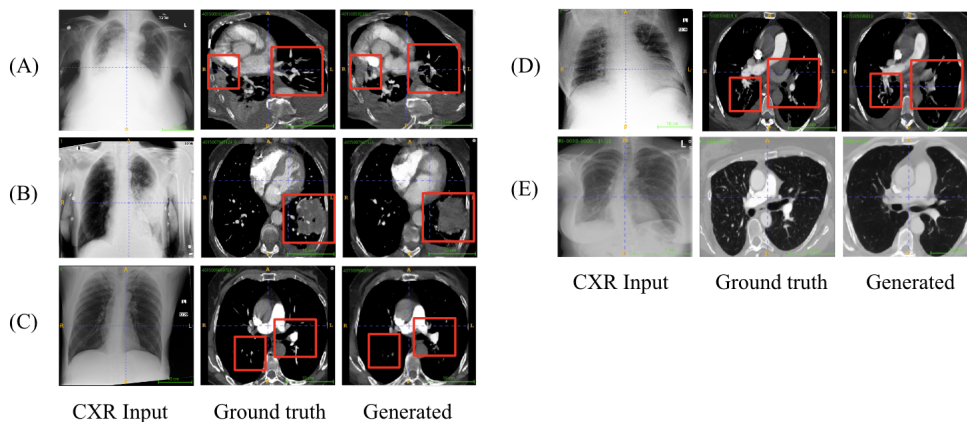


Figure 6. Failed Examples and Hallucinations. Presented are example slices from our test set where we consider the model to fail. (A) Moderate pleural effusions and kyphoscoliosis pathologies are apparent in both the CXR input and the ground truth sample. The generated sample shows the pleural effusions but they are not generated to be identical to the ground truth. (B) A lung cancer in the left lung is generated in the synthesized CTPA at the correct location and but is slightly different in texture and color. (C,D) Hallucinates the shape and locations of veins around the heart area. (E) Deformed right chest wall is absent.

Discussion

The purpose of this work was to generate 3D CTPA scans from paired 2D CXRs. To address this problem, we used a novel 3D diffusion model with BiomedCLIP Visual encoder, additional adversarial guidance, classifier and perceptual loss. We had many challenges when implementing this project: the number of samples in our dataset is relatively small, the size of each CTPA scan is large, the 3D nature of the CT scans enforces consistency throughout the generated 3D scan and between 2D slices which makes it hard to use the common 2D pretrained models. In addition, the 2D CXR data inputs are not registered or aligned to the CTPA scans. Finally, the application of PE is challenging due to the small size of the clots in the scans.

We were able to generate somewhat realistic, consistent and anatomically correct 3D scans. The generated 3D scans are not identical to the ground truth CTPAs but are similar and capture their structure. We experimented in the image size and additional modifications to the model and loss functions. Our best performing model improved the CXR PE classification results by 11%; Improving from an AUC of 0.691 [95% CI: 0.54-0.77] to 0.803 [95% CI: 0.72-0.9]. In addition, the specificity of the model improved, which in a clinical setting may potentially lead to a reduction of redundant CTPA scans performed for PE suspected patients. Unlike other diffusion studies in the medical field, this research uniquely applies generated data to address a real-life clinical challenge rather than focusing on the quality of the generated samples. As far as we know, this is the first model that attempts to convert 2D chest X-rays to CTPA scans. We also demonstrate the model's generalizability by fine-tuning it on an extremely small number of samples to achieve 2D CXR to 3D CT translation.

This study is subject to a few significant limitations. It was designed as a single-center, retrospective study, which is associated with well-known shortcomings and inherent limitations. In addition, generalizing the methods and results of our study to other predictive tasks with different modalities should be examined carefully, as our comparison and analysis were limited to CXR and CTPA modalities and to the task of PE classification. Finally, while our model generates 3D CTPA scans which are close to the ground truth, they are by no means identical to them and currently cannot be used to replace CTPA scans. This is shown throughout the paper, specifically, in the Failed examples Section, where we present examples of failure and model hallucinations. We hypothesize that in order for the generated scans to be used as actual replacements for the original CTPAs, we need a much larger dataset.

For future work, we intend to apply our model to alternative paired modalities to test the model’s ability to generalize to other domains. X-ray2CTPA demonstrates promising results in generating realistic and accurate 3D CTPA scans, paving the way for a future where AI-powered medical imaging can transform healthcare by making advanced diagnostic tools more accessible and affordable for patients worldwide.

Methods

X-ray2CTPA diffusion model

The limited number of samples in our dataset, their substantial size and 3D nature, were the main considerations for our model architecture selection. The model is constructed from a two-step approach: first, the images are encoded into a low-dimensional latent space using a frozen pretrained 2D-VAE and subsequently, a 3D diffusion probabilistic model is trained on the latent representation of the data. The compressed nature of the low-dimensional latent space inherently enables faster training and inference and alleviates the problem of limited computational resources. An outline of our model architecture is presented in Fig. 7.

We used the pretrained version of a 2D-VAE that was fine-tuned from the original kl-f8 autoencoder to improve the reconstruction of faces^{30,31}. The model remained frozen without any further fine-tuning for our dataset. The 3D-CTPA scans were fed to the 2D-VAE sequentially slice by slice and then concatenated before being fed into the 3D diffusion model. For the conditional setting, we added 2D CXR scans as conditioning to the diffusion model. We hypothesize that the CXR to CTPA modality shift is more like text to image conversion rather than image-to-image inpainting. Therefore, we applied the conditioning by concatenation of the CXR embedding throughout the 3D U-net layers, rather than applying it as concatenation to the noise as input of the U-net. The CXR was encoded to a 512-vector using BiomedCLIP Visual encoder³². We further improve the 3D scan generation by imposing a 4 layered 3D discriminator at the output of the diffusion process. In addition, a DenseNet3D-121³³ classification was also applied on the generated latents to introduce label information and improve classification results.

The 2D-VAE and BiomedCLIP Visual encoder remained frozen during the training and only the 3D diffusion model and the 3D discriminator were trained. Due to the small number of samples, we pretrained the diffusion model on the largest publicly available annotated PE dataset (RSPECT) - 2020 RSNA Pulmonary Embolism Detection Kaggle Challenge, which is comprised of more than 7,000 3D CTPA studies from five international research centers¹⁸.

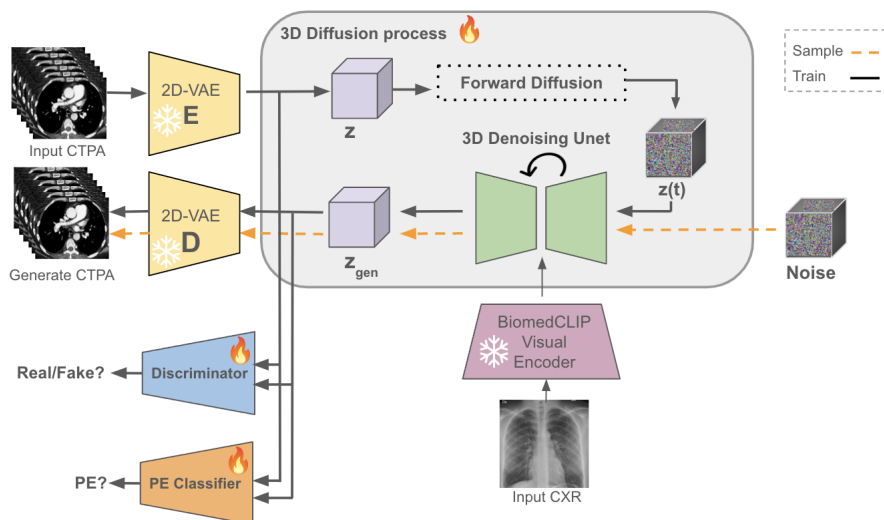


Figure 7. X-ray2CTPA model architecture: Black arrows - Training: The CTPA scan are fed slice by slice to the 2D-VAE in a sequential manner and compressed by a factor of 8. The compressed slices are concatenated. The latent representation is noised in the forward diffusion process and is then used as input to the 3D denoising U-net model. The CXR acts as conditioning to the model, fed into the CLIP Vision encoder. Bottom - Sampling: A noise latent and CXR are the inputs to the model and the output is the reconstructed 3D CTPA scan.

Dataset

Our cohort was constructed from 898 patients who underwent both a chest X-ray scan and a chest CT scan with contrast agent - CT pulmonary angiography (CTPA) within a 24-hour difference and from a single center. The chest CT volumes were annotated by board certified radiologists for a single label determining whether the patients had pulmonary embolism (PE) or not. The CTPA scans were anonymized and categorized by expert opinion indicating whether PE existed or not (no severity indication and no marked PE segmentation) according to the radiologist’s report. For the evaluation of the models, we used a stratified sixfold cross-validation. 305 of the samples (34 %) were marked positive for PE. The dataset specifications are presented in Table 5. An institutional review board (IRB) approval was granted for this work. Informed consent was waived by the IRB committee.

Table 5. Dataset specifications

Category	Numbers (%)
Total	898 (100 %)
Train	803 (89 %)
Validation	50 (6 %)
Test	45 (5 %)
Patients positive for PE	305 (34 %)
Patients negative for PE	593 (66%)

Data pre-processing

The 3D CTPA scans had a spacial resolution of 512×512 with varying number of axial slices. All scans were resampled to a standard uniform voxel spacing of 1 mm in all dimensions. The pixel values were converted to Hounsfield units (HU) and windowed to the range of $(-100HU, +900HU)$, to enhance the lower and upper boundaries of the area of interest limits of the HU scale. Finally, the scans were cropped to the region of the lung area using lung segmentation and resized to a size of 256x256x128 voxels (height x width x depth). Due to this preprocessing step, the axial slices of the scans seem a bit deformed. We min-max normalized the scans to the range of $(-1,1)$. To achieve a reduced length without additional spacial manipulation of the data, the scans were divided into two segments of 256x256x64 each by selecting every alternate slice. Additionally, we augmented all datasets by vertically flipping the images during training with a probability of 50%.

The 2D CXR scans were normalized and resized to the size of 224 x 224 x 3 to match the size of the BiomedCLIP Vision encoder³².

Loss functions

We utilize multiple loss functions to improve its training, each with a distinct purpose. The overall loss is a combination of l_1 , perceptual similarity (LPIPS)²⁴ weighted by λ_1 , a discriminator loss, weighted by λ_2 and a classification loss weighted by λ_3 . l_1 loss ensures the generated images closely match the ground truth. LPIPS, leveraging the 2D ResNet-50 based RadImageNet architecture²⁷, enhances the model’s grasp of complex semantic details and ensures perceptual similarity. The discriminator loss further ensures the generated images’ realism, and the classifier loss guides the samples to the PE classification task. $\lambda_1, \lambda_2, \lambda_3$ were set to 0.01, 0.001 and 0.08 respectively. The loss can be summarized as follows:

$$loss = l_1 + \lambda_1 * l_{LPIPS} + \lambda_2 * l_{adv} + \lambda_3 * l_{cls} \quad (1)$$

Statistical Analysis

The performance evaluation on the test set covered AUC, sensitivity (also known as recall), specificity, accuracy, the positive predictive value (PPV, also known as precision), and the negative predictive value (NPV). The DeLong method²⁶ was used to calculate the 95% confidence intervals for the AUC. The probability thresholds for predicting positive samples were determined by the sensitivities and specificities on the validation set, which ensured high specificities while keeping reasonable sensitivities. These thresholds were determined by Youden’s index³⁴, which finds the optimal joint sensitivity and specificity.

Implementation Details

All models were trained on a single NVIDIA RTX A5000 GPU, and each took about a week of training. The code for our model was based on Medical Diffusion¹¹ with various alterations. The training parameters included a base learning rate of

$1e^{-4}$ for the unconditional setting and when pretraining using RSPECT dataset and a learning rate of $1e^{-5}$ when fine-tuned for the final conditional model. An additional pretraining step was added in which we used the RSPECT dataset for pretraining but in a conditional setting. We used artificial CXR images or digitally reconstructed Radiographs (DRRs) as conditioning. The DRRs were created using DiffDRR³⁵ Python package for differentiable X-ray rendering. All were trained with a batch size of 2 with AdamW optimizer and Cosine Anneal scheduler. We used DDPM sampling with 1000 steps.

References

1. Pfeiffer, D., Pfeiffer, F. & Rummeny, E. Advanced x-ray imaging technology. *Recent Results Cancer Res* **216**, 3–30 (2020).
2. Ferrara, R. & Mansi, L. Paul suetens (ed): Fundamentals of medical imaging (2nd edition). *Eur. J. Nucl. Medicine Mol. Imaging* **38**, 409–409 (2011).
3. Lo, P. *et al.* Extraction of airways from ct (exact'09). *IEEE Trans Med Imaging* **31**, 2093–2107 (2012).
4. Righini, M., Robert-Ebadi, H. & Le Gal, G. Diagnosis of acute pulmonary embolism. *J Thromb Haemost* **15**, 1251–1261 (2017).
5. Hendy, A. *et al.* How good are gpt models at machine translation? a comprehensive evaluation. *arXiv preprint arXiv:2302.09210* (2023).
6. Ramdurai, B. The impact, advancements and applications of generative ai (2023).
7. Prevedello, L. M. *et al.* Challenges related to artificial intelligence research in medical imaging and the importance of image analysis competitions. *Radiol Artif Intell* **1**, e180031 (2019).
8. Ying, X. *et al.* X2ct-gan: reconstructing ct from biplanar x-rays with generative adversarial networks. In *Proceedings of the IEEE/CVF conference on computer vision and pattern recognition*, 10619–10628 (2019).
9. Corona-Figueroa, A. *et al.* Mednerf: Medical neural radiance fields for reconstructing 3d-aware ct-projections from a single x-ray. In *2022 44th Annual International Conference of the IEEE Engineering in Medicine & Biology Society (EMBC)*, 3843–3848 (IEEE, 2022).
10. Kazerouni, A. *et al.* Diffusion models for medical image analysis: A comprehensive survey. *arXiv preprint arXiv:2211.07804* (2022).
11. Khader, F. *et al.* Medical diffusion - denoising diffusion probabilistic models for 3d medical image generation, DOI: [10.48550/ARXIV.2211.03364](https://doi.org/10.48550/ARXIV.2211.03364) (2022).
12. Waibel, D. J., Röell, E., Rieck, B., Giryes, R. & Marr, C. A diffusion model predicts 3d shapes from 2d microscopy images. In *2023 IEEE 20th International Symposium on Biomedical Imaging (ISBI)*, 1–5 (IEEE, 2023).
13. Dorjsembe, Z., Pao, H.-K., Odonchimed, S. & Xiao, F. Conditional diffusion models for semantic 3d medical image synthesis. *arXiv preprint arXiv:2305.18453* (2023).
14. Zhu, L. *et al.* Make-a-volume: Leveraging latent diffusion models for cross-modality 3d brain mri synthesis. In *International Conference on Medical Image Computing and Computer-Assisted Intervention*, 592–601 (Springer, 2023).
15. Hamamci, I. E. *et al.* Generatect: Text-guided 3d chest ct generation. *arXiv preprint arXiv:2305.16037* (2023).
16. Paulson, B. *et al.* Xprospect: Ct volume generation from paired x-rays. *arXiv preprint arXiv:2403.00771* (2024).
17. Bourigault, E., Hamdi, A. & Jamaludin, A. X-diffusion: Generating detailed 3d mri volumes from a single image using cross-sectional diffusion models. *arXiv preprint arXiv:2404.19604* (2024).
18. Colak, E. *et al.* The rsna pulmonary embolism ct dataset. *Radiol Artif Intell* **3**, e200254 (2021).
19. Dhariwal, P. & Nichol, A. Diffusion models beat gans on image synthesis. *Adv. neural information processing systems* **34**, 8780–8794 (2021).
20. Salimans, T. *et al.* Improved techniques for training gans. *Adv. neural information processing systems* **29** (2016).
21. Yang, Z., An, G., Zhang, R., Zheng, Z. & Ruan, Q. Sri3d: Two-stream inflated 3d convnet based on sparse regularization for action recognition. *IET Image Process.* **17**, n/a–n/a, DOI: [10.1049/ipr2.12725](https://doi.org/10.1049/ipr2.12725) (2022).
22. Horé, A. & Ziou, D. Image quality metrics: Psnr vs. ssim. In *2010 20th International Conference on Pattern Recognition*, 2366–2369, DOI: [10.1109/ICPR.2010.579](https://doi.org/10.1109/ICPR.2010.579) (2010).
23. Wang, Z., Bovik, A., Sheikh, H. & Simoncelli, E. Image quality assessment: from error visibility to structural similarity. *IEEE Transactions on Image Process.* **13**, 600–612, DOI: [10.1109/TIP.2003.819861](https://doi.org/10.1109/TIP.2003.819861) (2004).

24. Zhang, R., Isola, P., Efros, A. A., Shechtman, E. & Wang, O. The unreasonable effectiveness of deep features as a perceptual metric. In *Proceedings of the IEEE conference on computer vision and pattern recognition*, 586–595 (2018).
25. Zhang, L., Rao, A. & Agrawala, M. Adding conditional control to text-to-image diffusion models. In *IEEE International Conference on Computer Vision (ICCV)* (2023).
26. DeLong, E. R., DeLong, D. M. & Clarke-Pearson, D. L. Comparing the areas under two or more correlated receiver operating characteristic curves: a nonparametric approach. *Biometrics* **44**, 837–845 (1988).
27. Mei, X. *et al.* Radimagenet: An open radiologic deep learning research dataset for effective transfer learning. *Radiol Artif Intell* **4**, e210315 (2022).
28. Armato, S. G. r. *et al.* The lung image database consortium (lidc) and image database resource initiative (idri): a completed reference database of lung nodules on ct scans. *Med Phys* **38**, 915–931 (2011).
29. Hu, E. J. *et al.* Lora: Low-rank adaptation of large language models (2021). [2106.09685](https://arxiv.org/abs/2106.09685).
30. Rombach, R., Blattmann, A., Lorenz, D., Esser, P. & Ommer, B. High-resolution image synthesis with latent diffusion models (2021). [2112.10752](https://arxiv.org/abs/2112.10752).
31. Blattmann, A., Rombach, R., Oktay, K. & Ommer, B. Retrieval-augmented diffusion models, DOI: [10.48550/ARXIV.2204.11824](https://doi.org/10.48550/ARXIV.2204.11824) (2022).
32. Zhang, S. *et al.* Large-scale domain-specific pretraining for biomedical vision-language processing. *arXiv preprint arXiv:2303.00915* (2023).
33. Huang, G., Liu, Z., van der Maaten, L. & Weinberger, K. Q. Densely connected convolutional networks (2018). [1608.06993](https://arxiv.org/abs/1608.06993).
34. YODEN, W. J. Index for rating diagnostic tests. *Cancer* **3**, 32–35, DOI: [10.1002/1097-0142\(1950\)3:1<32::aid-cnrc2820030106>3.0.co;2-3](https://doi.org/10.1002/1097-0142(1950)3:1<32::aid-cnrc2820030106>3.0.co;2-3) (1950).
35. Gopalakrishnan, V. & Golland, P. Fast auto-differentiable digitally reconstructed radiographs for solving inverse problems in intraoperative imaging. In *Workshop on Clinical Image-Based Procedures*, 1–11 (Springer, 2022).
36. Clark, K. *et al.* The cancer imaging archive (tcia): maintaining and operating a public information repository. *J. digital imaging* **26**, 1045–1057 (2013).

Acknowledgements

The research in this publication was supported by the Israel Science Foundation (ISF) under grant number 20/2629.

Declarations

Funding. This study was funded by the Israel Science Foundation (ISF) under Grant number 20/2629.

Conflict of interest/Competing interests. The authors have no relevant financial or non-financial interests to disclose.

Consent for publication. The IRB committee of Sheba Medical Center waived the need of informed consent.

Data availability. The CXR-CTPA dataset generated and/or analysed during the current study are not publicly available due patient privacy regulations but are available from the corresponding author on reasonable request. The LIDC-IDRI (<https://wiki.cancerimagingarchive.net/pages/viewpage.action?pageId=1966254>) dataset is publicly available at the cancer imaging archive (TCIA)³⁶.

Code availability. The code and models generated in this study are available: <https://github.com/NoaCahan/X-ray2CTPA>.

Author contributions statement

Guarantor of integrity of the entire study, planning and supervision, E.K, G.A, H.G.; data curation or data analysis/interpretation, E.K, Y.B.; study concepts/study design and methodology, N.C, R.G, H.G.; software, visualization and writing of the original draft N.C.; Clinical consulting G.A., E.K.; manuscript drafting or manuscript revision for important intellectual content, all authors.; approval of final version of submitted manuscript, all authors.; agrees to ensure any questions related to the work are appropriately resolved, all authors.; literature research, N.C., Y.B.; experimental studies, N.C, R.G, H.G.; statistical analysis, N.C., R.G., H.G.; and manuscript editing, R.G, N.C, E.K, E.K, Y.B, H.G.